Polymer 81 (2015) p. 1-11
DOI: 10.1016/j.polymer.2015.11.007

Linking the morphology of a high hard segment content polyurethane to its thermal behaviour and mechanical properties

Y. Swolfs[1], E. Bertels[2], I. Verpoest[1,3], B. Goderis[2,3]

[1] Department of Materials Engineering, KU Leuven, Kasteelpark Arenberg 44 bus 2450, 3001 Leuven, Belgium

[2] Department of Chemistry, KU Leuven, Celestijnenlaan 200F, 3001 Leuven, Belgium

[3] Leuven Material Research Centre (Leuven-MRC), KU Leuven

Abstract

Understanding and controlling the morphology of thermoplastic polyurethane (TPU) is crucial, as it is closely linked with its thermal and mechanical properties. The morphology of a TPU with a high hard segment content was investigated. When hard segment crystallisation was avoided by fast cooling, a crystallisation-induced phase separation occurred upon reheating. At higher temperatures, a second polymorph was additionally created. Cooling slowly from the melt directly induced the formation of both polymorphic forms. The complex thermal behaviour could hence be explained by the (cold) crystallisation and melting of two polymorphs. The disordered two-phase nanomorphology, revealed by AFM at room temperature after cooling slowly, was validated for both fast and slowly cooled samples at higher temperatures by fitting model SAXS patterns to time resolved synchrotron SAXS data. Annealing fast cooled samples at high temperature induced some ordered, lamellar stacks in addition. Finally, the morphology was linked to the evolution of storage modulus with increasing temperature.

Email address: yentl.swolfs@mtm.kuleuven.be (Y. Swolfs)

Keywords: Morphological modelling; Thermoplastic polyurethane; Storage modulus

1 Introduction

Thermoplastic polyurethanes (TPU) are widely used in industrial applications, such as foam and sports equipment, and have attracted considerable research interest. TPUs are linear segmented copolymers, consisting of alternating soft and hard segments. The hard segments (HS) tend to separate from the soft segments (SS) by their crystallisation or do so in the liquid state due to a thermodynamic incompatibility with the soft segments.

Phase-separated aromatic diphenylmethane diisocyanate (MDI) TPUs often adopt a lamellar nano-morphology even though several authors reported different morphologies. Spherical or cylindrical morphologies [1] have been reported in MDI extended with ethylene diamine, while a morphology without a specific shape was reported for MDI extended with 2-methyl-1,3-propane diol [2] or with butane diol [3]. The TPU morphology affects the mechanical properties [4, 5]. The hard domains act as physical cross-links and reinforce the TPU in a similar fashion to nano-fillers. The reinforcement efficiency is increased when the HS fraction increases and the hard domains are more interconnected [6]. Alternatively, the TPU reinforcement increases when also the SS phases crystallise [7].

The TPU nanomorphology is commonly visualised by Atomic Force Microscopy (AFM) [8-10] or Transmission Electron Microscopy (TEM) [2, 5]. However, as these techniques are

Polymer 81 (2015) p. 1-11
DOI: 10.1016/j.polymer.2015.11.007
rarely operational at elevated temperatures, (synchrotron) Small Angle X-ray Scattering (SAXS) is the often the method of choice for investigations of the nano-morphology as a function of temperature. Conversely, the interpretation of SAXS data relies on the use of a suitable morphological model, which is nine times out of ten based on microscopic observations. SAXS and microscopy are thus highly complementary. The thermal behaviour of TPUs is commonly studied by Differential Scanning Calorimetry (DSC), which also yields information on the TPU morphology, albeit indirectly. Relations between thermal behaviour and morphology are often studied by DSC in conjunction with (synchrotron) Wide Angle X-ray Diffraction (WAXD) and SAXS [2, 11-16]. The size and position of the thermal transitions varies with thermal history [12, 13], mechanical deformation [14], composition ratio [15] and soft segment length [16].

An intriguing thermal feature of MDI TPUs is the multiple melting endotherms. Early literature [17, 18] attributed these endotherms to different types of hydrogen bonds, where the urethane NH bond is the donor, and either the urethane carbonyl or the macrodiol is acting as acceptor. This hypothesis was later rejected by Samuels & Wilkes [19], who investigated a TPU without hydrogen bonding and proved that the explanation of hydrogen bonding is insufficient. Therefore, alternative explanation were coined, based on various levels of packing order [11, 20, 21]. These authors suggested that the low temperature endothermic peak was associated with disordering of the short range order and the high temperature one to the disordering of the long range order. The final peak was attributed to the melting of the microcrystalline order. Apart from the multiple melting endotherms, TPUs also exhibit annealing endotherms. They occur at 20-50 °C above the annealing temperature [11, 16, 22, 23]. During heating towards the annealing temperature or at the annealing temperature, some of the ordered structures will melt. Fluid segments that revert to the solid state must be stable at the annealing temperature and will melt above the annealing temperature. Higher annealing temperatures result in larger annealing induced endotherms, as more material is melted and re-arranged.

This paper explores the morphology of MDI TPU with high HS content and 1,6-hexane diol as chain extender as a function of the applied cooling rate and the annealing parameters. The link between the processing induced morphology and the thermal and mechanical properties (the storage modulus in particular) is investigated.

2 Experimental

2.1 Materials

All research was conducted on Irogran D74 P 4742E by Huntsman. This is a polyether-based TPU with high hard segment content. The polyether is a polytetrahydrofuran with brandname Terathane and molecular weight of 1000. The isocyanate is 4,4'-methylene diphenyl diisocyanate (MDI) with brand name Suprasec 1306. The chain extender is 1,6-hexanediol. The HS content is 73.5 wt%, if all MDI and 1,6-hexanediol are counted as hard segment.

The TPU pellets were dried 24 h at 80 °C in a vacuum of less than 5 mbar. This ensured a thorough drying of the pellets. The pellets were poured in a frame of 250x250x2 mm. This was put in between two aluminium foils, treated with Chemlease PR-90. The entire setup was put in between a hot press at 220 °C and a pressure of 10 bar was applied during the entire cycle. After 10 min at 220 °C, the samples were cooled down according to the cooling profile in Figure 1. The sample was removed when the temperature dropped below 50 °C. This sample is called the reference sample. Some of these samples were annealed for 72 h in an oven, either at 100 °C or 150 °C. The samples were then removed from the oven and cooled

Polymer 81 (2015) p. 1-11
DOI: 10.1016/j.polymer.2015.11.007
to room temperature on a steel surface. The same production procedure was also performed at a constant cooling rate of 0.5 °C/min. For this material, no extra annealing steps were applied. This sample is called the slowly cooled sample.

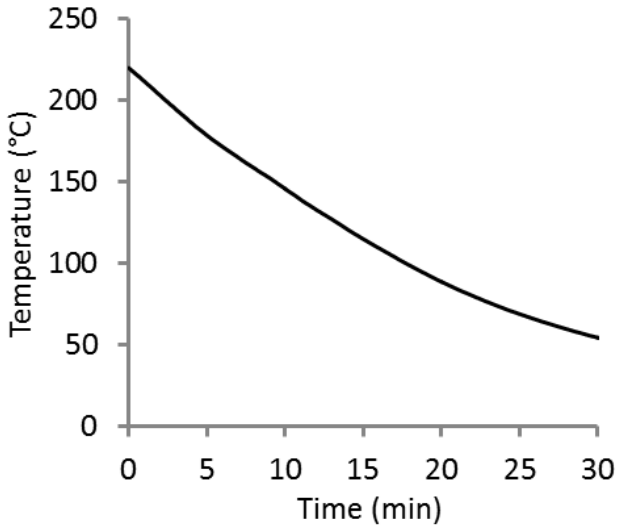

Figure 1: Temperature profile for the cooling of the reference samples.

2.2 Differential scanning calorimetry

For the DSC measurements, a DSC Q2000 (Universal V4.3 TA Instruments) was used, with aluminium TZero lidded pans from TA Instruments. Samples of about 3 mg were cut from pressed plates. The measuring unit was flushed with 25 ml N_2/min during all experiments. Heating and cooling rates were 10 °C/min in all cases. The endo- and exothermic peak temperatures correspond to the maxima of the transitions, whereas the glass transitions were calculated as the inflection point. The enthalpy values were measured relative to the baseline. Examples of these baselines will be shown later in Figure 4.

2.3 X-ray scattering

Time-resolved Small Angle X-ray Scattering (SAXS) and Wide Angle X-ray Diffraction (WAXD) measurements using synchrotron radiation were performed on the Dutch-Flemish (DUBBLE) beam line BM26B at the European Synchrotron Radiation Facility (ESRF) in Grenoble (France). The experiments were executed at a fixed wavelength λ of 1.24 Å. A 2D multiwire gas-filled detector, with a 13 by 13 cm area and pixel size of 250 µm, was placed at 2.5 m from the sample after an evacuated tube for measuring the SAXS. The known reflections of silverbehenate were used to calibrate the scattering angles, expressed in terms of q, with $q = 4\pi sin\theta/\lambda$ and θ being half the scattering angle. The setup enabled measuring SAXS intensities in the range from q = 0.0133 Å^{-1} to q = 0.265 Å^{-1}, corresponding roughly to structures having a size from $2\pi/q$ = 470 Å to 24 Å. WAXD data were collected simultaneously at a position close to the sample on a 2D VHR CCD detector from Photonic Science. The WAXD intensities were measured in the range q = 0.7 Å^{-1} to q = 2.45 Å^{-1}, corresponding to sizes from 2.56 Å to 9 Å. Scattering angles were calibrated using a polyethylene sample.

The SAXS and WAXD patterns were normalised to the intensity of the incoming beam, measured by an ionisation chamber placed downstream from the sample. The scattering patterns were corrected for the detector response and in the WAXD case additionally for the

Polymer 81 (2015) p. 1-11
DOI: 10.1016/j.polymer.2015.11.007
dark current prior to azimuthally averaging the isotropic data using home-made software [24]. Both the SAXS and WAXD patterns were corrected for the scattering due to the empty setup, taking into account sample and sample holders transmission differences. The SAXS and WAXD intensities are both represented as a function of *q*.

2.4 Atomic force microscopy

Atomic force microscopy imaging was carried out in Tapping Mode™ with a Multimode™ Veeco system, operating with a Nanoscope IV™ Veeco controller and E- type scanner. An Olympus silicon Micro Cantilever with a resonance frequency of about 250 kHz was used. The measurements were carried out on TPU samples prepared in an oven at 220 °C. A constant cooling rate of 0.5 °C/min was applied. Hence, a slowly cooled sample was created and imaged. Teflon sheets were put on the top and bottom instead of release agent. The sample surface was scanned without further treatment.

2.5 Dynamic Mechanical Analysis

A dynamic mechanical analyser DMA Q800 of TA Instruments was used for testing all the samples. The rectangular samples have a size of 50x12.5x2 mm, and were tested in three-point bending mode. The frequency was set to 1 Hz, while the applied strain was 0.05%. The samples were first cooled to -80 °C, before starting the heating cycle. The heating and cooling rate was always 2 °C/min. The glass transition temperature was taken as the temperature at the middle of the drop in storage modulus.

2.6 Interpretation of the SAXS data

For interpreting the SAXS patterns of TPUs, a lamellar domain structure is often assumed. As explained in the introduction, this is not always adequate [1, 2, 25]. Figure 2 schematically depicts two morphologies, which – as will be demonstrated in the results section – are relevant to the present system. In these morphologies, the black areas cover 26.5% of the total area and represent the volume occupied by the SS phases, assuming complete phase separation from the white areas, which represent the HS volumes. The percentage occupancy is in line with the chemical composition, i.e. 73.5 wt% HS, and disregards differences between weight and volume fractions. Within the white areas, the blue inclusions represent HS crystalline material, which in A occupies 40% of the HS phase and in B 60%. It is assumed that SAXS is dominated by the electron density contrast between the HS and SS domains and that hence the electron density difference between crystalline and amorphous HS volumes is rather small compared to the difference between SS and HS regions.

The HS phases in morphology A of Figure 2 are not lamellar and dispersed within the SS matrix. However, as the SS phases are rather thin, they still can be considered as layer-like, say lamellar. Morphology B of Figure 2 is closer to the classical lamellar case where HS and SS phases alternate in a one dimensional stack. The stacks are, however, rather short and the lateral dimensions very limited.

Polymer 81 (2015) p. 1-11
DOI: 10.1016/j.polymer.2015.11.007

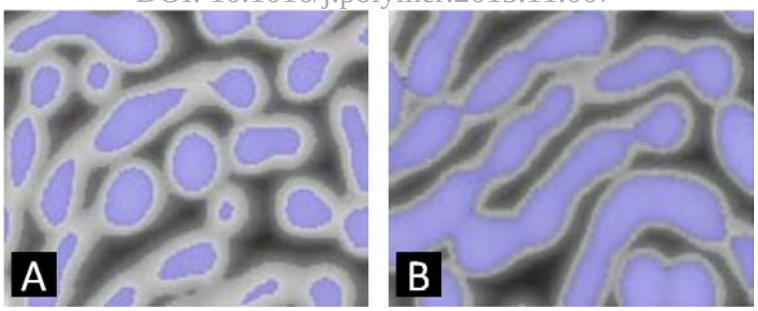

Figure 2: Schematic representation of potential TPU morphologies with the black and white areas corresponding to respectively the soft and hard segment phases. The blue inclusions within the white areas correspond to crystallites within the hard segment phases. In morphology A, the hard segment phases do not adopt lamellar structures whereas the morphology in B approaches the classical lamellar case with alternating HS and SS layers in a one dimensional stack.

The SAXS intensity function $I_{dis}(q)$ for disordered morphologies such as the ones in Figure 2A and 2B and anything in between, can be calculated as [26]:

$$I_{dis}(q) = \frac{C \cdot \alpha \cdot (\rho_H - \rho_S)^2 \left[F(q)\right]^2}{4 \cdot \pi \cdot q^2} + D \,. \tag{1}$$

The parameter C depends on the irradiated volume and the beam intensity. The parameters ρ_H and ρ_S are the electron densities of the hard and soft segment phases respectively. α is the volume fraction of two-phase regions. Large mixed regions are assumed to not contribute to the observed SAXS intensity [27]. The factor D takes into account the background caused by local electron density fluctuations. The scattered wave function $F(q)$ of the underlying one dimensional electron density profile corresponds to:

$$\begin{aligned} F(q) = 2 \cdot \frac{\ell_S}{L_P} \cdot \frac{\sin\left(q \cdot L_P / 2\right)}{q} \cdot \exp\left(-\frac{\sigma_{LP_{dis}}^2 \cdot q^2}{2}\right) \\ - 2 \cdot \frac{\sin\left(q \cdot \ell_S / 2\right)}{q} \cdot \exp\left(-\frac{\sigma^2 \cdot q^2}{2}\right) \end{aligned} \tag{2}$$

The overall one dimensional electron density profile, producing scattering as described by equation 1, can be understood as the average electron density profile, seen from the centre of the SS layers with monodisperse thickness, ℓ_S. This profile evolves from a central SS layer over the next neighbour HS phase to the system average density, $\langle\rho\rangle$. The smoothness of the SS sigmoidal transition is governed by σ, that of the HS transition by $\sigma_{LP_{dis}}$. The total thickness of the transition zones equals 3σ and $3\sigma_{LP_{dis}}$ respectively. The parameter L_p corresponds to twice the distance from the centre of the amorphous layer to the point at which the electron density, $\rho(x)$, reaches $\langle\rho\rangle$ for the case $\sigma_{LP_{dis}} = 0$. With this parameter, the volume fraction of the SS phase, ϕ_S, can be defined as

$$\phi_S = \frac{\ell_S}{L_P} \tag{3}$$

Polymer 81 (2015) p. 1-11
DOI: 10.1016/j.polymer.2015.11.007

Obviously, $(1-\phi_S)$ equals the HS phase volume fraction, ϕ_H, and as a result <ρ>, is given by

$$\langle\rho\rangle = \phi_S \cdot \rho_S + (1-\phi_S)\cdot\rho_H \tag{4}$$

Figure 3 visualises L_p and ℓ_S for $\sigma_{LP_{dis}}$ = 0 and for $\sigma_{LP_{dis}}$ = $(L_P - \ell_S)/3$, the limiting case for which ℓ_S remains unaffected by the width of the transition to <ρ> [26].

Equation 1 was suggested earlier to model disordered morphologies in semicrystalline starch [26]. Note that <ρ> does not appear explicitly in equation 1, whereas this is the case in the equivalent of equation 1 given in [26]. This difference originates from inserting the equations (3) and (4) in the equation given in [26]. This allowed putting the factor $(\rho_H - \rho_S)^2$ in front of $[F(q)]^2$. Finally, as a correction to [26], the σ-containing factor is included within $F(q)$.

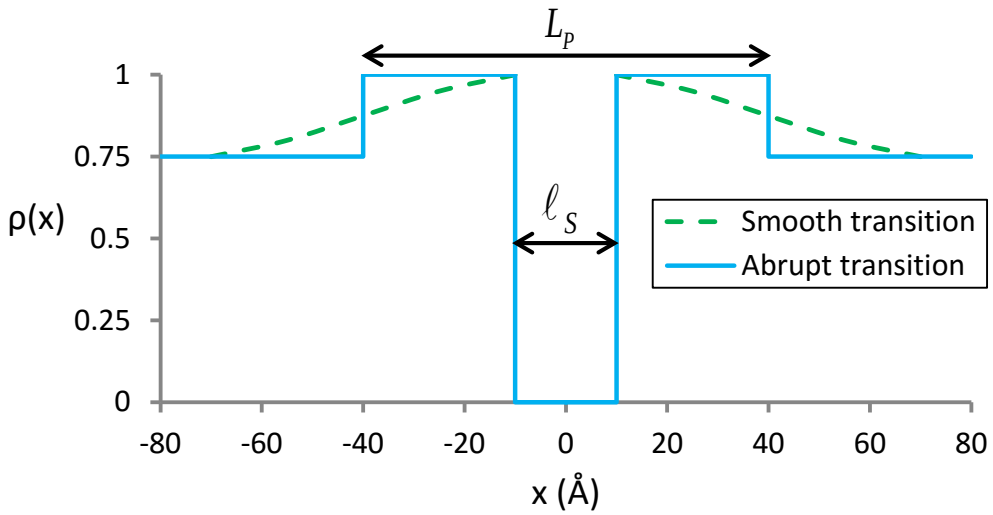

Figure 3: Schematic representation of the electron density functions associated with equation (1) with σ = 0 and $\sigma_{LP_{dis}}$ = 0 (blue curve) or $\sigma_{LP_{dis}}$ = $(L_P - \ell_S)/3$ (green dashed curve). A zero σ value implies a sharp transition between the central soft segment phase (ρ(x) = 0) and the high density hard segment phases (ρ(x) = 1). The evolution from the hard segment phase density to the system average value (ρ(x) = 0.75) is sharp for the blue curve and limiting smooth for the green dashed curve.

The SAXS intensity function $I_{ord}(q)$ for an ordered two-phase morphology composed of alternating lamellae is given by [26]:

$$I_{ord}(q) = \frac{C\cdot\alpha\cdot(\rho_H-\rho_S)^2}{4\cdot\pi\cdot q^2}\left[\frac{2\cdot\sin\left(\frac{q\cdot\ell_S}{2}\right)}{q}\right]^2\cdot S(q)\cdot\exp\left(-q^2\cdot\sigma^2\right)+D \tag{5}$$

The factor between square brackets is the form factor for the SS layers, which are assumed to have a monodisperse thickness of ℓ_S. The function $S(q)$ is the interference function of the paracrystalline positioning of the soft segment layers and is calculated as:

Polymer 81 (2015) p. 1-11
DOI: 10.1016/j.polymer.2015.11.007

$$S(q)=\frac{1-\exp\left(-q^2\cdot\sigma_{LP_{ord}}^2\right)}{1+\exp\left(-q^2\cdot\sigma_{LP_{ord}}^2\right)-2\cdot\exp\left(-0.5\cdot q^2\cdot\sigma_{LP_{ord}}^2\right).\cos\left(q\cdot L_P\right)} \tag{6}$$

The standard deviation of the average stacking periodicity L_p for such lamellarly ordered morphologies is given by $\sigma_{LP_{ord}}$. To avoid negative L_p values within the distribution, the ratio $\sigma_{LP_{ord}}/L_P$ should be less than 0.4. The average HS phase thickness equals $L_P-\ell_S$ and is characterised by a distribution identical to that of L_p.

The *q* value at which equation (5) produces a maximum in $I_{ord}(q)$ is closely related to L_p via Bragg's Law, in particular when $\sigma_{LP_{ord}}$ is low. The scattered intensity given by equation (1) also produces a peak at a given *q* value, but the relation with L_p is not trivial [26].

The TPU morphology can also be intermediate between the disordered and lamellarly ordered cases. Such a morphology, with a scattered intensity $I_{\text{int}}(q)$, can be modelled by a linear combination of equations 1 and 5:

$$I_{\text{int}}(q)=\frac{C\cdot\alpha\left(\rho_H-\rho_S\right)^2}{4\cdot\pi\cdot q^2}\cdot\left[(1-\beta)\left[F(q)\right]^2+\beta\cdot\left[\frac{2\cdot\sin\left(\frac{q\cdot\ell_S}{2}\right)}{q}\right]^2\cdot S(q)\cdot\exp\left(-q^2\cdot\sigma^2\right)\right]+D \tag{7}$$

where β is the fraction of lamellarly ordered and $(1-\beta)$ the fraction of disordered volumes. The two fractions are modelled to have the same hard segment fraction by using identical ℓ_S and L_p values to describe the ordered and disordered fractions. As a result, the potential scattering due to ordered and disordered volumes is contrast-matched and does not contribute to the SAXS intensity.

The experimental SAXS data for the reference and slowly cooled samples were fitted to equation 1. This was performed by a least-squares minimisation of the logarithmic errors. To obtain this fit, six parameters were allowed to vary: $C\cdot\alpha_S.\left(\rho_H-\rho_S\right)^2$, D, ℓ_S, L_P, $\sigma_{LP_{dis}}$ and σ. The thickness σ of the transition zone was set to zero to ensure a stable fit, reducing the effective number of variables to five. The standard deviation $\sigma_{LP_{dis}}$ of the average stack periodicity was constrained to be smaller than $(L_P-\ell_S)/3$. This constraint ensures that the relative density $\rho(x)$ reaches ρ_H at its maximum.

Only *q*-values below $q = 0.214$ Å^{-1} were used in the optimisation to avoid interference with the WAXD data. All parameters were allowed to vary as a function of temperature. The initial guess of the solution at each temperature was equal to the solution at the previous temperature. In the case of both reference and slowly cooled samples, a good fit was achieved

Polymer 81 (2015) p. 1-11
DOI: 10.1016/j.polymer.2015.11.007
with equation 1, which is indicative for disordered morphologies. Electron density profiles, such as illustrated in Figure 3, can then be calculated by inverse Fourier transformation of the scattered wave function $F(q)$:

$$\rho(x) = \langle\rho\rangle + \frac{1}{2\cdot\pi}\int_0^\infty 2\cdot F(q)\cdot\cos(q\cdot x)\cdot dq\,. \tag{8}$$

For this calculation ρ_H and ρ_S were set equal to 1 and 0 respectively, as their absolute values cannot be extracted from the lumped fitting parameter $C\cdot\alpha\cdot(\rho_H-\rho_S)^2$. For that reason the computed electron densities will be referred to as apparent electron densities. Note that only half of the electron density profiles are displayed in the discussion session. Adding a mirror pattern at the negative x-axis side would yield the full profiles, similar to the schematic one in Figure 3. At high x-values $\rho(x)$ reaches $\langle\rho\rangle$. Given equation (4) and the fact that ρ_H and ρ_S are set to 1 and 0, the apparent $\langle\rho\rangle$ equals the SAXS-based hard segment volume fraction.

3 Results

3.1 Thermal transitions during heating

Figure 4 presents the heat capacity DSC thermograms. In the reference sample, five peaks can be distinguished, labelled as T_I, T_{II}, T_{III}, T_{IV}, T_V. On top of that, the glass transition at about 40 °C is indicated by the dashed line. The temperature and enthalpy of all transitions are summarised in Table 1.

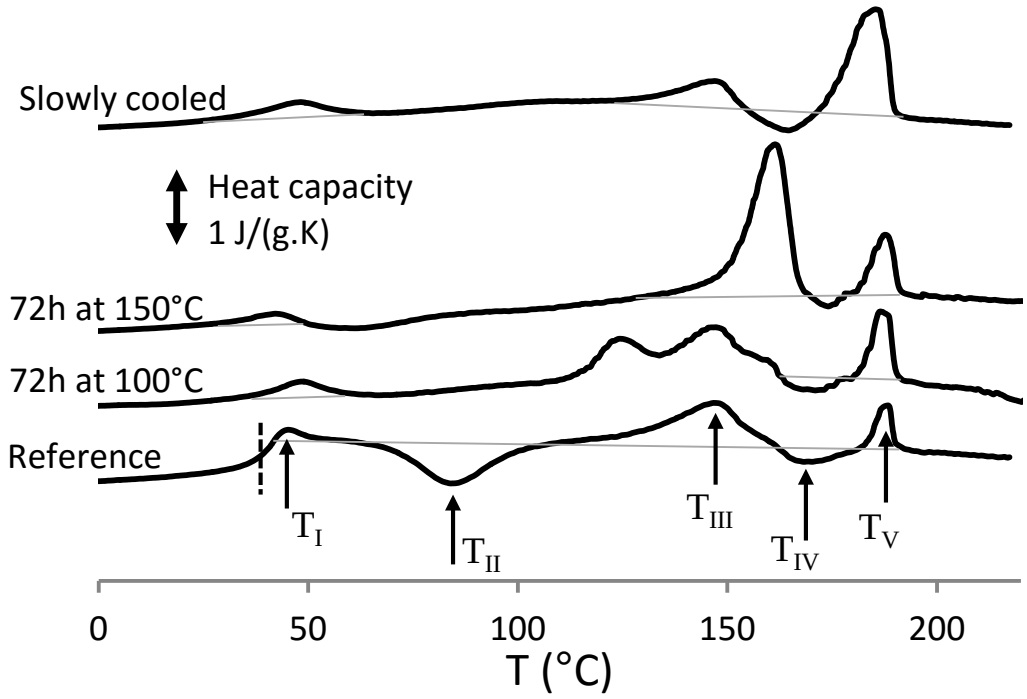

Figure 4: DSC heat capacity thermograms for the four studied samples. The relevant temperatures for the reference sample are indicated by arrows. The dashed line indicates the location of the glass transition for the reference system, which was obtained by cooling rather rapidly and which resulted in a mixed system. The thin grey line indicates the baseline that was used to calculate the enthalpy values.

Polymer 81 (2015) p. 1-11
DOI: 10.1016/j.polymer.2015.11.007

Table 1: Temperature and enthalpy of the thermal transitions in the four studies samples. Not all transitions were present in all samples, and the T_{III} transition for the sample annealed at 100°C could not be determined reliably due to the partial overlap with an annealing endotherm.

		T_g	T_I	T_{II}	T_{III}	T_{IV}	T_V
Reference	Temperature (°C)	37.3 ± 0.5	45.3 ± 0.4	84.7 ± 1.5	148.2 ± 0.8	166.6 ± 1.0	188.8 ± 0.6
	Enthalpy (J/g)	none	1.3 ± 0.1	11.1 ± 1.7	9.4 ± 1.7	1.5 ± 0.2	4.6 ± 1.2
72h at 100°C	Temperature (°C)	n/a	46.9 ± 4.5	n/a	n/a	167.3 ± 1.1	186.8 ± 0.3
	Enthalpy (J/g)	none	2.5 ± 0.6	n/a	n/a	2.9 ± 0.6	5.5 ± 0.3
72h at 150°C	Temperature (°C)	n/a	43.2 ± 1.7	n/a	160.9 ± 1.5	174.0 ± 0.2	187.4 ± 0.8
	Enthalpy (J/g)	none	2.2 ± 0.5	n/a	20.9 ± 2.7	2.2 ± 0.4	4.6 ± 0.8
Slowly cooled	Temperature (°C)	n/a	47.6 ± 1.5	n/a	147.2 ± 0.6	163.8 ± 1.7	184.9 ± 1.3
	Enthalpy (J/g)	none	4.1 ± 0.5	n/a	3.2 ± 1.0	3.5 ± 1.8	15.0 ± 4.5

Figure 5 displays WAXD and SAXS measurements on the reference sample at selected temperatures to evaluate the morphology and phase behaviour as a function of temperature. At room temperature, crystalline peaks or shoulders are absent in the WAXD-pattern at 29 °C in Figure 5b. Crystallisation was hence avoided by the fast cooling. Furthermore, it can be deduced from the featureless SAXS pattern at 29 °C (see Figure 5a) that the TPU segments remained fully mixed. In other words, there are no indications for a liquid-solid or a liquid-liquid type of microphase separation. This morphology stays valid even after T_I, indicating that the T_I endotherm is due to enthalpic recovery at devitrification. This was also demonstrated by Wilhelm and Gardette for a hexanediol-MDI TPU, albeit with a different polyether [28].

The T_{II} exotherm is a crystallisation-induced phase separation. This is proven by two facts. Firstly, three small shoulders are visible in the WAXD pattern at 120 °C in Figure 5b, which is after the T_{II} exotherm. These crystallites with reflections at d-spacing of 3.8 Å, 4.1 Å and 5.1 Å will be labelled polymorph A for the remainder of this paper. The fact that the shoulders are difficult to observe, proves that the crystallinity is low and/or that the crystals themselves are small and/or of little internal order. Secondly, a SAXS peak is observed in Figure 5a at 120 °C. This is attributed to a phase separation into HS and SS rich phases.

The microphase separation remains after the endothermic signal at T_{III}, although different in nature as the SAXS peak has shifted to smaller *q* values (see the 164 °C pattern in Figure 5a). Furthermore, the type A WAXD shoulders seem to have weakened at 164 °C compared to at 120 °C, suggesting A-type crystal melting in the T_{III} endotherm (see Figure 5b). Not all A-type crystals, however, melt at this event, as (very faint) remnants of the reflections remain up to higher temperatures. At 164 °C, the first signs of a second crystalline polymorph start appearing. This second polymorph, with its single reflection at a d-spacing of 4.7 Å (indicated with a dotted line in Figure 5b) will be labelled polymorph B.

Blackwell and Lee [14] also detected two polymorphs in an hexane diol-MDI TPU and proved that they were both triclinic. Similarly, D'Hollander et al. [29] found two polymorphs in their TPU: a triclinic form having multiple diffraction peaks and a pseudo-hexagonal one with a single reflection at 4.2 Å. Polymorphs with a single strong reflection (cfr. polymorph B) are quite often due to the pseudo-hexagonal packing of stretched-out polymer chain with a cylindrical symmetry due to (frozen in) rotational freedom along the polymer chain axis. Crystal structures with well-defined chain packing readily produce multiple reflections (cfr. polymorph A). Polymorph A and B thus represent crystals with respectively high and low short range order.

Polymer 81 (2015) p. 1-11
DOI: 10.1016/j.polymer.2015.11.007
The WAXD intensity associated with the polymorph B gains importance during the small exotherm at T_{IV}. This exotherm thus seems to be related to B type crystal formation. At T_V, all WAXD peaks and shoulders disappear, which indicates all hard segments melt. The long range order completely disappears, which corresponds to the absence of the A and B polymorphs. Concomitantly, the SAXS intensity collapses as illustrated for 205°C, proving that the hard and soft segments fully remix. When analysing the WAXD patterns in more depth, the polymorph A remnants seems to disappear before polymorph B and already during the T_{IV} exotherm. As a result, the WAXD pattern at 180 °C only contains the B type reflection, besides a pronounced amorphous halo.

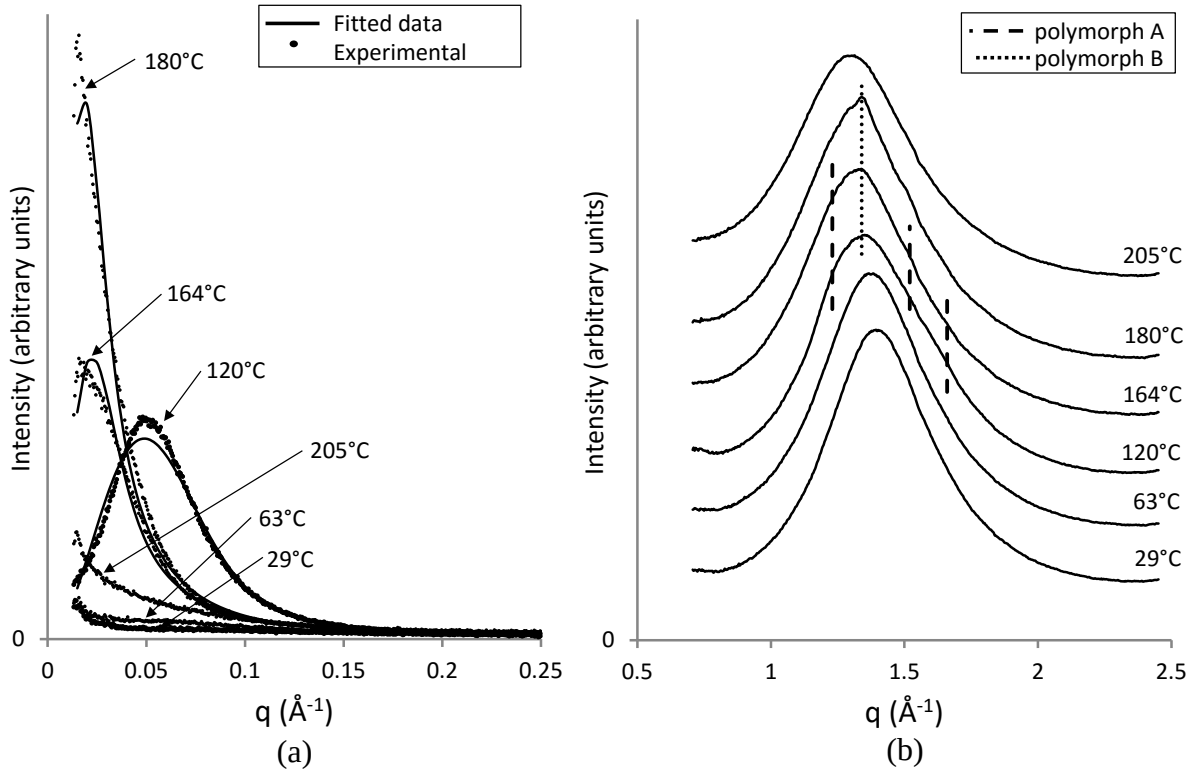

Figure 5: (a) SAXS and (b) WAXD patterns of the reference sample. For the SAXS data, both the experimental and fitted (using equation 1) data are plotted. The fits for 29 °C, 63 °C and 205 °C are not presented as the segments are homogeneously mixed at these temperatures. The WAXD data are shifted over the intensity axis for the sake of clarity.

3.2 Thermal transitions during heating after slow cooling

When the sample is cooled down slowly, the morphology at room temperature is drastically different. During slow cooling, the HS have enough time to crystallise, which causes them to separate from the SS. The SAXS peak in Figure 6a at 34 °C reveals that phase separation has indeed occurred. Furthermore, the A as well as the B polymorph are clearly present at room temperature (Figure 6b).

Since crystallisation-induced phase separation has already occurred, the exothermic peak at T_{II} no longer appears (see Figure 4). The endothermic transition at T_{III} remains and is again related to the partial melting of A-type crystals. The reduction of A type crystals can be inferred from a comparison of the 34 °C WAXD pattern with the ones at 155 °C or 181 °C. The patterns at 155 °C and 181°C were taken above the T_{III} transition and clearly reveal weaker type A reflections. In SAXS, a small decrease in $C \cdot \alpha \cdot (\rho_H - \rho_S)^2$ will be observed at

Polymer 81 (2015) p. 1-11
DOI: 10.1016/j.polymer.2015.11.007
T_{III} as a result of the creation of mixed regions and hence a reduction of α. Details of the SAXS shape analysis will be presented and discussed in section "3.4 Morphology".

At the T_{IV} exotherm, further growth of the B type crystals occurs as can be deduced from the sharper B type reflection in the 181 °C WAXD pattern compared to at 155 °C. Concomitantly, the SAXS peak strongly shifts to lower *q* values. Again, all crystals melt at the T_V peak as deduced from the collapsing SAXS intensities and WAXD crystalline reflections at 203°C in Figure 6. Further investigation revealed that polymorph A and B disappear rather simultaneously, but that ultimately only the B type crystals remain prior to completion of the melting process. The long range order as probed by SAXS disappears completely when the last polymorph B crystals have melted.

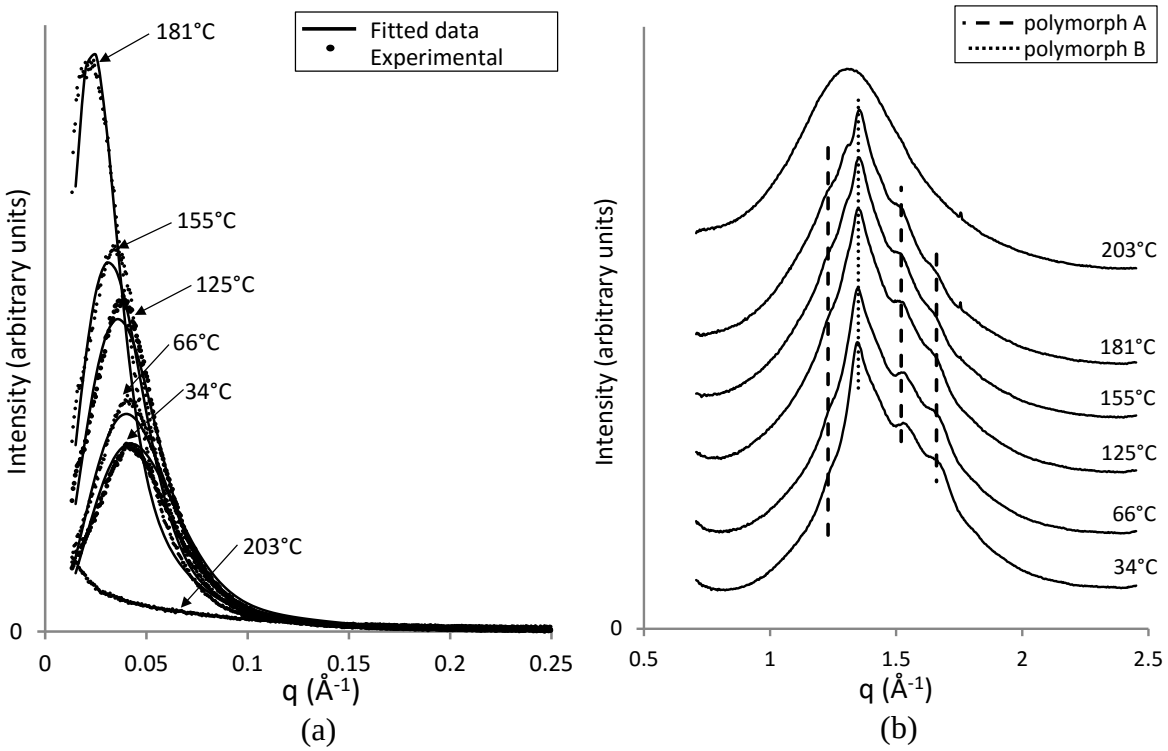

Figure 6: (a) SAXS and (b) WAXD patterns of the slowly cooled sample. For SAXS, both the experimental and fitted (using equation 1) data are plotted. The fit for 203 °C is not presented as the segments are homogeneously mixed at this temperature. The WAXD data are shifted over the intensity axis for the sake of clarity.

3.3 Thermal transition during heating after annealing the reference samples

The influence of annealing the reference sample is revealed in Figure 7. The WAXD patterns prove the development of polymorph A. Furthermore, the small shoulders after annealing at 100 °C become more pronounced after annealing at 150 °C. Note that the low angle WAXD reflection is slightly shifted to higher *q* values (q = 1.29 Å^{-1}) compared to after cooling slowly (q = 1.23 Å^{-1}). This may point at A type crystals with a higher density after annealing. Polymorph B is not present in the samples. For the reference sample, polymorph B develops within the T_{IV} exothermic peak, which occurs above 150 °C. Hence, the annealing temperature was not high enough to develop polymorph B. The phase separation in the annealed samples is clear from the SAXS data in Figure 7a. At higher annealing temperatures, structures have evolved to larger length scales, as the SAXS peak has shifted to smaller angles. Note that fitting to equation 1 yields poor reproductions of the experimental SAXS

Polymer 81 (2015) p. 1-11
DOI: 10.1016/j.polymer.2015.11.007
patterns, indicating that the morphology cannot be described by this limiting case of high disorder. An alternative fitting will be discussed in section "3.4 Morphology".

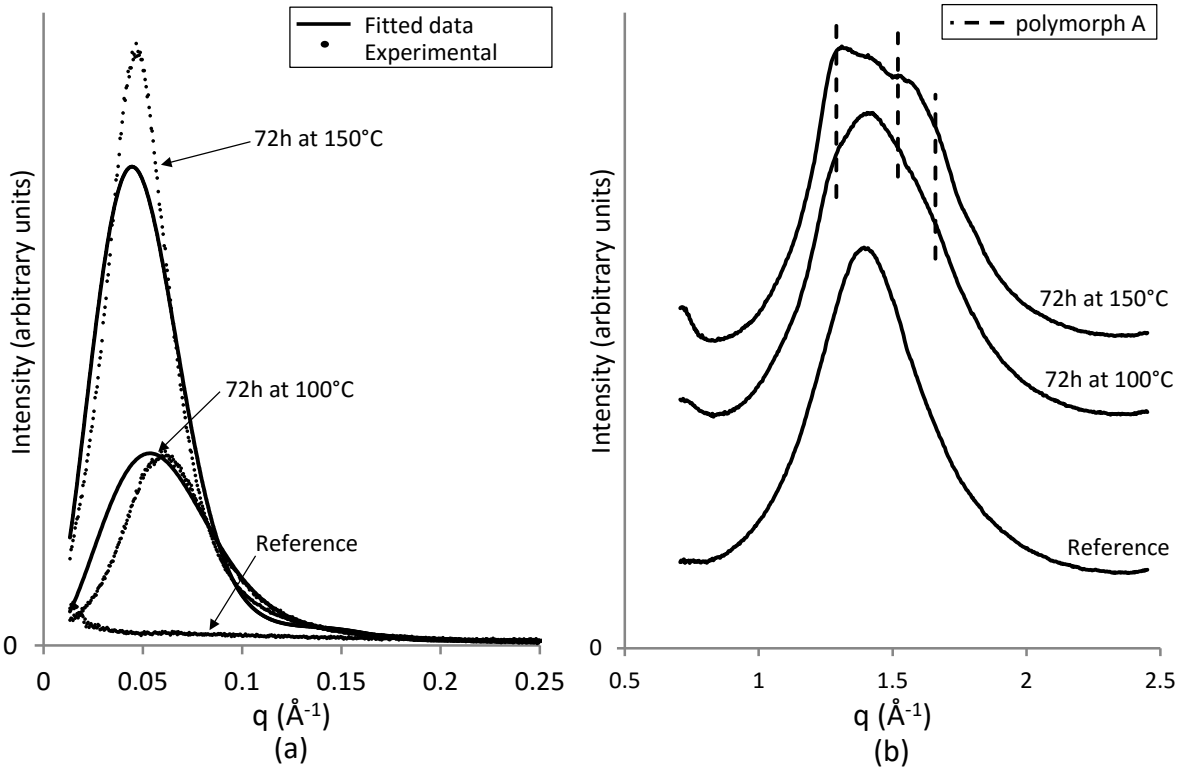

Figure 7: (a) SAXS and (b) WAXD patterns of the reference sample before and after annealing. These data were collected at room temperature, after cooling down from the annealing temperature. For SAXS, both the experimental and fitted (using equation 1) data are plotted. The fit for the reference sample is not presented as the segments are homogeneously mixed at this temperature. The WAXD data are shifted over the intensity axis for the sake of clarity.

All samples were stored at room temperature for at least 24h before the DSC measurements were started. This results in an enthalpic recovery endotherm T_I around 40 °C in all samples (see Figure 4). T_{II} is absent in both annealed samples because the phase separation has already occurred during the annealing or during heating up to the annealing temperature.

The sample annealed at 100 °C developed a new DSC peak at 125 °C. This is an annealing endotherm and most likely represents the melting of very small A-type crystals that are only stable up to temperatures just above the annealing temperature where they were created. Unfortunately, no time-resolved X-ray data was available for the annealed samples to verify this hypothesis. At higher temperatures, the thermal behaviour of the sample annealed at 100 °C closely resembles that of the reference sample and should be understood in similar terms.

The annealing endotherm is also present in the sample annealed at 150 °C. In that case, however, the peak joins the T_{III} peak, which is shifted to higher temperatures and larger compared to in the other samples. Annealing a fast cooled sample at 150 °C seems to produce a higher amount of more perfect A type crystals compared to when no annealing was allowed. The perfection of these A type crystals is however lower compared to the majority of the A type crystals that were formed during slow cooling. This can be deduced from the sharper type A reflection after slow cooling (Figure 6b) as well as from the fact that the most stable A type crystals after cooling slowly, survive up to very high temperatures and melt within the

Polymer 81 (2015) p. 1-11
DOI: 10.1016/j.polymer.2015.11.007
broader T_V endotherm where also the B type crystals melt. Clearly, after cooling fast (reference sample) and irrespective of the annealing protocols, B type crystals are only generated in the T_{IV} exotherm and melt in the T_V endotherm. Once the majority of A–type crystals melted in the T_{III} endotherm, the three systems arrive at a comparable state prior to enrolling into the T_{IV} and T_V DSC signals (see Figure 4 and Table 1). Accordingly, these signals for the sample annealed at 150 °C are comparable with those of the reference samples or the sample annealed at 100 °C.

3.4 Morphology

Before analysing the temperature dependent SAXS data, a microscopic view of the morphology is needed to verify the suggested models. Figure 8 presents the AFM phase image of a slowly cooled sample. The Teflon sheet topography too strongly contributed to the height image, hampering its analysis (data not shown). The most conspicuous 100 nm features in the phase image relate to what made the height image uninformative. The features of interest are highlighted by artificial colouring in the 500 nm box within Figure 8. A disordered morphology can be observed similar to the one in Figure 2B. The layer-to-layer distances in the brighter patches fall between 150 and 300 Å. The SAXS data of the reference and slowly cooled samples were hence fitted to equation 1. Representative fits are displayed in the Figures 5 and 6, illustrating that the data was fitted well. The data with larger deviations between experiment and fit will not be shown or discussed. At those temperatures, the morphology was not sufficiently developed yet.

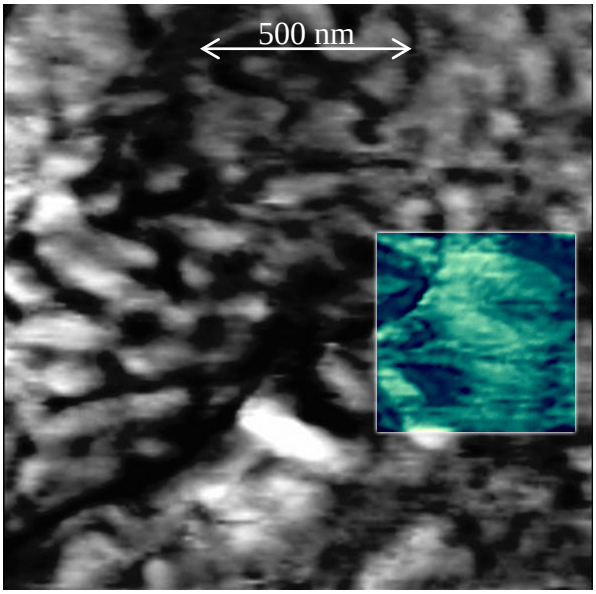

Figure 8: AFM phase image at room temperature of a slowly cooled sample. The phase angle runs from 0 (black) to 4° (white). The inset is artificially coloured for better visualisation.

Figure 9 presents one wing of the related apparent electron density profiles of the reference and slowly cooled TPU as a function of temperature. The corresponding parameters, ℓ_S, L_P, $\sigma_{LP_{dis}}$, ϕ_H and $C \cdot \alpha \cdot (\rho_C - \rho_A)^2$ are presented in Figure 10. The parameter D is of little interest. For the reference sample, the functions and parameters below 114 °C and above 191 °C are left out. Section "3.1 Thermal transitions during heating" proved that no phase separation exists below 60 °C. Even though phase separation developed between 60 °C and 114 °C, the patterns below 114°C were too ill-defined to ensure a good fit. Above 191 °C, the

Polymer 81 (2015) p. 1-11
DOI: 10.1016/j.polymer.2015.11.007
SAXS patterns collapsed due to complete melting and segment remixing. For the slowly cooled sample, data are presented up to 191°C for the same reason.

It is convenient to first discuss the SAXS based morphological development during heating after cooling slowly because this represents the simplest case. In the temperature range before the T_{III} endotherm, except for devitrification, nothing seems to happen in DSC (Figure 4). In Figure 10, the SAXS parameters in this temperature range remain rather constant, except that ℓ_S, L_p and $C \cdot \alpha \cdot (\rho_H - \rho_S)^2$ slightly increase. This is most likely due to thermal expansion with the SS phases expanding more rapidly than the HS phases such that the factor $(\rho_H - \rho_S)^2$ increases. C and α presumably remain constant in this temperature range. Furthermore, the HS phase fraction, ϕ_H, probed by SAXS in this range amounts to 80%, which exceeds the mass based HS chemical share, i.e. 73.5 %. Assuming a higher density for the HS phase, one would expect a lower, rather than a higher HS SAXS based volume fraction if the phase separation were complete. It thus seems that part of the SS moieties are included within the HS volumes and hence that phase separation is incomplete even after slow cooling. For sure, the WAXD data in Figure 6 do not suggest a crystallinity of 80%, implying that the HS volumes are only partially crystalline and that morphologies similar to Figure 2 apply with the hard and soft phase morphology dominating over the morphology established by the crystalline regions in SAXS.

In the region associated with the T_{III} endotherm, ℓ_S and L_p continue to increase, albeit at a somewhat higher rate. Concomitantly, $C \cdot \alpha \cdot (\rho_H - \rho_S)^2$ drops to 80% of the original level (80% line in Figure 10e). Given that the temperature dependence of $(\rho_H - \rho_S)^2$ is rather small (as deduced from the behaviour in the low temperature region) and assuming that C remains constant over the entire experiment, it seems that α decreases. This is associated with the melting of A type crystals (cfr. the WAXD data discussed above) and a homogenisation of about 20% of the volume into volume elements that are large enough to escape the SAXS observation [27]. This reasoning builds on the idea that originally, the entire material volume was nanoscale phase separated (100% line in Figure 10e). The increase of ℓ_S, L_p and ϕ_H might be due to the preferential melting of regions with the lowest HS fraction and the smallest crystals, by which the average values as probed by SAXS increase. This is in agreement with thermodynamic principles, stating that larger crystals are more stable.

According to the same reasoning, the observed value for $\langle \rho \rangle$ corresponds to the average density of the remaining phase separated regions rather than of the entire system. Alternatively, the upward drift of ϕ_H further away from the chemically expected fraction, might be a result of a partial (re)mixing of the SS with HS at the T_{III} endotherm within the remaining phase separated regions. A remixing of the SS with the HS should lead to approaching ρ_H and ρ_S values. Indeed, a decrease in ρ_H can be calculated by using equation 4 and assuming that $\langle \rho \rangle$ equals the chemical composition and ρ_S zero at all time. Calculating $(\rho_H - \rho_S)^2$ based on the so calculated ρ_H value with ρ_S set to zero, learns that the decrease in $(\rho_H - \rho_S)^2$ by this effect in the T_{III} region is smaller than the increase due to differential thermal expansion as estimated from the behaviour of $C \cdot \alpha \cdot (\rho_H - \rho_S)^2$ at low temperature. The drops in $C \cdot \alpha \cdot (\rho_H - \rho_S)^2$ at T_{III} is therefore realised by a decrease of α rather than by

Polymer 81 (2015) p. 1-11
DOI: 10.1016/j.polymer.2015.11.007

changes in $(\rho_H - \rho_S)^2$. Accordingly, the scenario in which ℓ_S, L_p and ϕ_H increase by the preferential melting of regions with the lowest HS fraction and the smallest crystals is most realistic. Following this line of thought, the initial ϕ_H value of 80% (instead of the chemically expected lower value) may indicate the presence of homogeneous SS enriched regions that do not contribute to the observed SAXS, rather than a partial mixing of the segments in all regions. In that case, α would be slightly lower than 1 also at the lowest temperatures.

Within the T_{IV} exothermic region, the increase of ℓ_S, L_p and ϕ_H continues whereas $C \cdot \alpha \cdot (\rho_H - \rho_S)^2$ remains rather constant. Changes, such as the growth of B type crystals (which could contribute to the increase of L_p and ϕ_H) thus happen within the remaining semicrystalline regions. In the T_V endothermic zone, $C \cdot \alpha \cdot (\rho_H - \rho_S)^2$ evolves similarly as in the T_{III} endothermic region, reflecting the melting of A and B type crystals together with a remixing of the different segments. The increase of ϕ_H in this temperature range again suggests that the regions with the highest HS fraction and the largest crystals (mirrored in L_p being large) melt the latest.

Figure 9b presents the apparent electron density functions of the slowly cooled TPU. The transition from the crystalline density to the average density is smoothened out as the temperature increases. This effect is mainly caused by the increasing average electron density of the (remaining) two phase regions by the local HS excess therein. The growth of B crystals during the heating run also contributes as mentioned above.

Once the crystallisation induced phase separation has been established during the exothermic signal at T_{II}, SAXS probes a ϕ_H value of 78% (Figure 10d) for the reference sample at 114°C. This value is slightly below the 80% of the slowly cooled sample, but still above what can be expected from the chemical composition, suggesting incomplete phase separation or the existence of homogeneous SS enriched regions that escape the SAXS observation. Large scale segregation more readily happens at higher temperatures and when the crystallisation rate is rather low such as during slow cooling. During cold crystallisation at T_{II}, very little time for segregation is allowed. One can therefore expected less large scale segregation, accordingly less regions that do not contribute to the SAXS and hence a ϕ_H value closer to what is chemically expected. At 114°C, the morphology is finer compared to after slow cooling as both ℓ_S and L_p are smaller for the reference sample. Furthermore, the slightly lower $C \cdot \alpha \cdot (\rho_H - \rho_S)^2$ of the slowly cooled compared to for the reference sample at 114°C (and assuming comparable ρ_H and ρ_S values for the two cases) indicates that α for the reference is slightly larger. In other words: there are less SS enriched regions that do not contribute to the SAXS for the reference sample. Although C is not known in absolute terms, it can be defended that the C values for both samples are identical as normalisations were performed to the intensity of the direct beam measured by an ionisation chamber downstream from the sample.

Recall that the crystallinity at this temperature for the reference sample is much lower than for the slowly cooled material (see the WAXD patterns in Figure 5b and Figure 6b). The SAXS parameters thus again suggest that the SAXS signal is dominated by phase separated morphology, rather than by the crystallinity of the material. Following this reasoning, the morphologies in Figure 2A and 2B would scatter equally strong in SAXS although their

Polymer 81 (2015) p. 1-11
DOI: 10.1016/j.polymer.2015.11.007
crystallinities are different. Figure 2A most likely is a fairly rather realistic representation of the finer morphology of the reference sample, whereas Figure 2B inclines to the case after slow cooling. The very broad WAXD reflections for the reference sample (see Figure 5) point at small, disconnected crystallites as in Figure 2A whereas the narrower peaks for the slowly cooled sample are indicative for larger, more connected crystallites as in Figure 2B.

During the endotherm at T_{III}, $C \cdot \alpha \cdot (\rho_H - \rho_S)^2$ of the reference strongly decreases due to the melting of A type crystals and the ensuing remixing of segments. A higher fraction of A type crystals melts compared to after cooling slowly. Only 36% of the sample volume remains phase separated whereas this was 80% for the slowly cooled sample (see Figure 10d). Concomitantly, ℓ_S, L_p and ϕ_H increase, suggesting that HS-rich regions with larger crystallites survive. In this case, the change of these parameters might also reflect remixing processes within the remaining separated regions. Part of this internal remixing process is indeed reversed at the creation of B type crystals in the temperature region towards and at the exotherm at T_{IV} . In this region, ℓ_S and L_p decrease again whereas ϕ_H decreases. $C \cdot \alpha \cdot (\rho_H - \rho_S)^2$ remains unaffected, suggesting that the recrystallisation into B type crystals predominantly happens in A crystalline regions that melted the latest. This is conceivable, as larger A type crystallites leave larger HS enriched regions, which more readily nucleate B type crystallites. At temperatures intermediate between T_{III} and T_{IV}, $\sigma_{LP_{dis}}$ increases steeply. This may reflect a wide distribution in HS phase sizes and shapes. A similar increase is seen for the slowly cooled sample in the T_V endotherm where most of the material melts. For the reference sample at T_V, features are visible that remind of what happened during the T_{III} endotherm. This is expected for a continued melting and remixing process.

The apparent electron density functions of the reference TPU in Figure 9b are comparable to for the slowly cooled material. The flattening of the profiles, however, happens at lower temperatures where the A type crystal melt at T_{III}.

Polymer 81 (2015) p. 1-11
DOI: 10.1016/j.polymer.2015.11.007

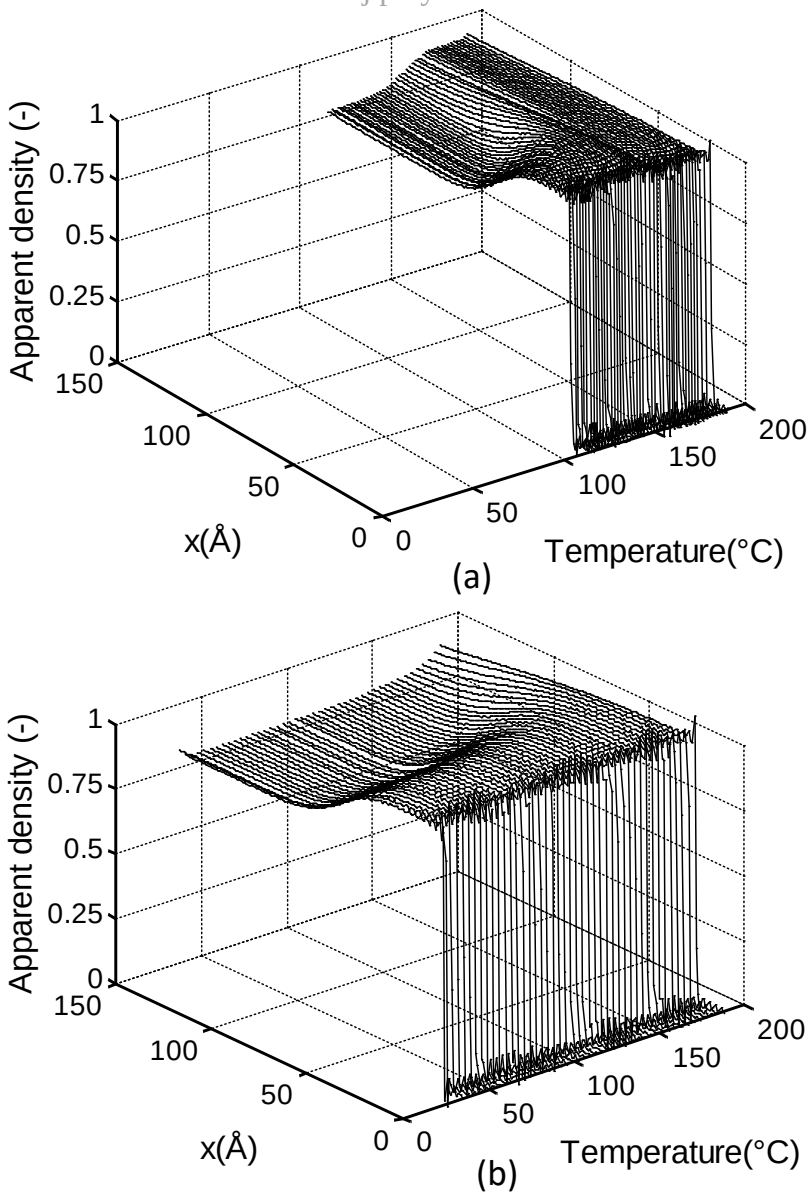

Figure 9: The apparent electron density profiles $\rho(x)$ for (a) the reference and (b) slowly cooled TPU in temperature ranges where the fits were reliable.

Polymer 81 (2015) p. 1-11
DOI: 10.1016/j.polymer.2015.11.007

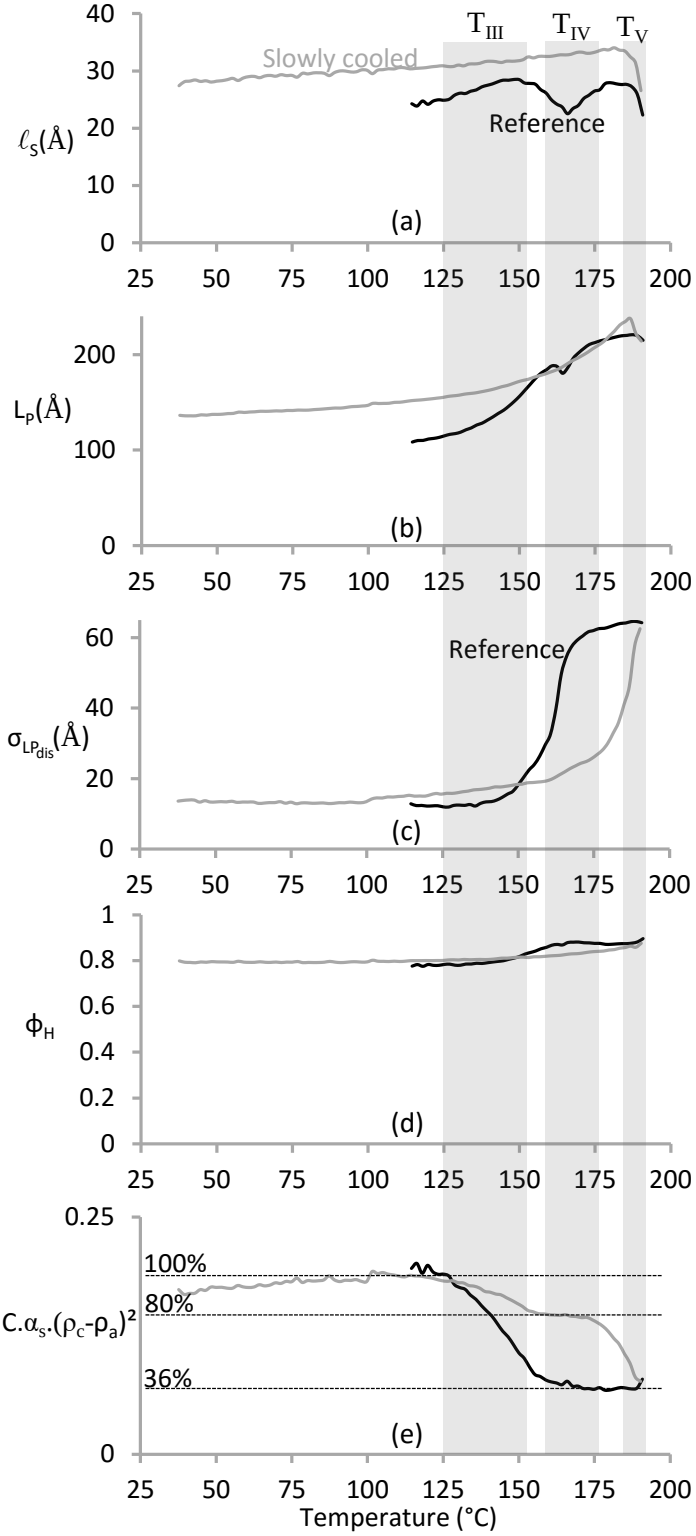

Figure 10: Evolution of (a) ℓ_S, (b) L_p, (c) $\sigma_{LP_{dis}}$, (d) ϕ_H, and (e) $C \cdot \alpha \cdot (\rho_H - \rho_S)^2$ as a function of temperature for the reference (black curves) and slowly cooled (grey curves) sample and based on a fitting of the SAXS patterns to equation 1. The vertical transparent bands demarcate the temperatures ranges of the T_{III}, T_{IV}, T_V thermal transitions. The horizontal dashed lines are helpful to the discussion (see text).

Equation 1 was not able to fully describe the morphology of the annealed TPUs as the experimental SAXS peaks are too sharp. Therefore, a fitting was made using equation 7. For this fitting, two new parameters were added to the five optimisation parameters used earlier:

Polymer 81 (2015) p. 1-11
DOI: 10.1016/j.polymer.2015.11.007

$\sigma_{LP_{ord}}$ and β. The results of these fits are illustrated in Figure 11. For the sample annealed at 100 °C, a reasonable fit was obtained by including 10% of a lamellarly ordered morphology (see Figure 11a). This increased to 15% for the sample annealed at 150 °C (see Figure 11b), indicating that more ordered structures can form at higher annealing temperatures. For the sample annealed at 100°C, ϕ_H equals 78%, just like for the reference sample right after the T_{II} exotherm. Also the ℓ_S and L_p values are comparable, i.e. 21 and 100 Å respectively. The originally formed dispersed small crystallites and domains thus (partially) merge laterally during annealing into lamellae while preserving the separation length scale in the stack direction. After annealing at 150°C, however, ϕ_H decreased down to 76% and ℓ_S and L_p rose to 32 and 127 Å respectively. The morphological coarsening thus seems to have progressed further after annealing at 150°C compared to after annealing at 100°C since the distances in the stack direction have also grown. Secondly, the lower ϕ_H value suggests that regions that remained mixed after cold crystallisation of the reference also phase separated at 72 hours 150°C. All in all, annealing increases the crystallinity and improves the HS phase connectivity. The DSC peak at T_V (see Figure 4) seems to be somewhat larger after annealing compared to for the reference sample, indicating a more efficient conversion to B type crystals after annealing. This can be due to the larger and more connected HS phases by which more readily (larger) B-type crystals can be generated at high temperature.

Note that $\sigma_{LP_{dis}}$ was found to be zero in both annealed samples. This suggests that the morphology is truly intermediate between disordered and lamellarly ordered.

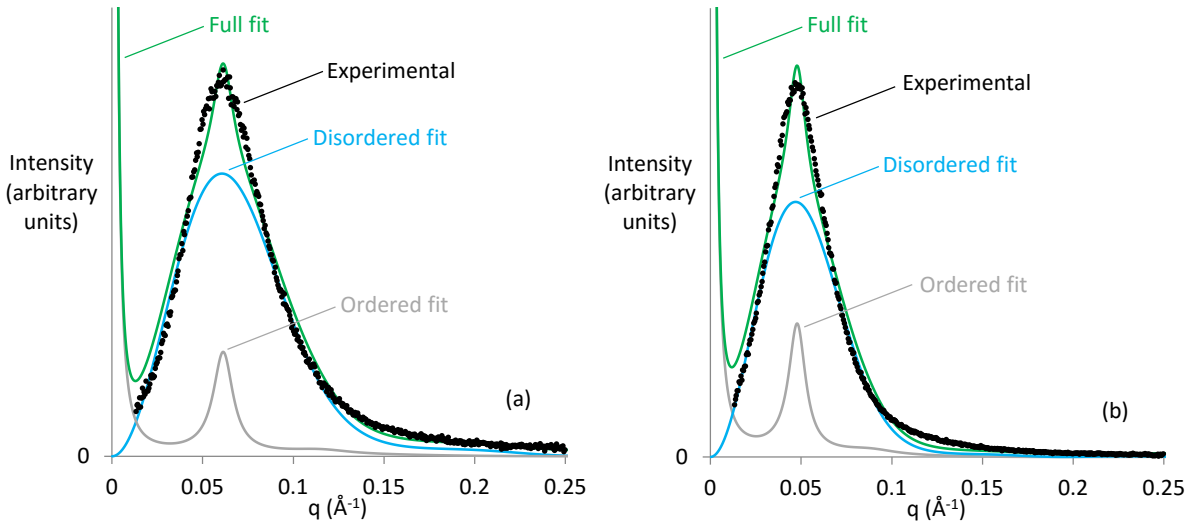

Figure 11: Fit with equation 7 (green line) to the experimental SAXS patterns (dots) for the reference TPU annealed for 72 hours at (a) 100 and (b) 150°C. The disordered and (lamellarly) ordered shares are represented in blue and grey lines respectively.

3.5 Influence on storage modulus

Figure 12 illustrates the storage modulus of the four sample types. The reference sample is not phase separated yet at room temperature. Therefore, the reference sample stays reasonably stiff below the glass transition temperature of the mixed phase around 40 °C. Next, the sample displays elastomeric behaviour. The crystallisation-induced phase separation starts around 60°, corresponding to the onset of the T_{II} peak in Figure 4. This transition changes the TPU morphology from a fairly soft amorphous polymer above its glass transition temperature to a

Polymer 81 (2015) p. 1-11
DOI: 10.1016/j.polymer.2015.11.007
phase separated polymer with a domain structure. These crystalline domains act as physical cross-links between the liquid chains and increase the modulus by this crosslinking as well as by the stiffness increase associated with crystallisation.

In the annealed and slowly cooled samples, the crystallisation-induced phase separation has already occurred. This gives a lower modulus value just below the glass transition of the mixed reference system, because the phases enriched in SS devitrify earlier. This effect is not so obvious in the DSC data in Figure 4, likely because devitrification happens over a rather large temperature range. Phase separation for the slowly cooled and annealed samples also yields a higher modulus at temperatures above the glass transition temperature of the mixed phase. The HS enriched region may devitrify later because of their own nature, but also because of being connected to HS crystallites. These HS keep the modulus relatively high after the main glass transition temperature.

The modulus of the reference only increases once crystallisation sets in at the T_{II} exotherm. However, the reference modulus never reaches the value of the slowly cooled or annealed samples. This might be due to the lower crystallinity as well as the presence of dispersed, rather than connected HS phases. A large fraction of the crystallites formed by annealing at 100°C melt during the annealing endotherm at about 130°C by which the modulus tumbles down to the reference value. The modulus up to the onset of the T_{III} endotherm for the sample annealed at 150°C or after cooling slowly remains rather high. Interestingly, a higher modulus is seen for the sample annealed at 150°C compared to after cooling slowly. The slowly cooled sample contains a large fraction of B-type crystals (see Figure 6b) whereas the sample annealed at 150°C only contains A type crystals (see Figure 7b). The large endotherm close to T_{III} for the sample annealed at 150°C suggests that its crystallinity is relatively high, and likely higher than of the slowly cooled sample. The sharpness of the WAXD peaks suggests more perfect crystallites for the slowly cooled sample, but it seems that the crystalline fraction is more important to the modulus.

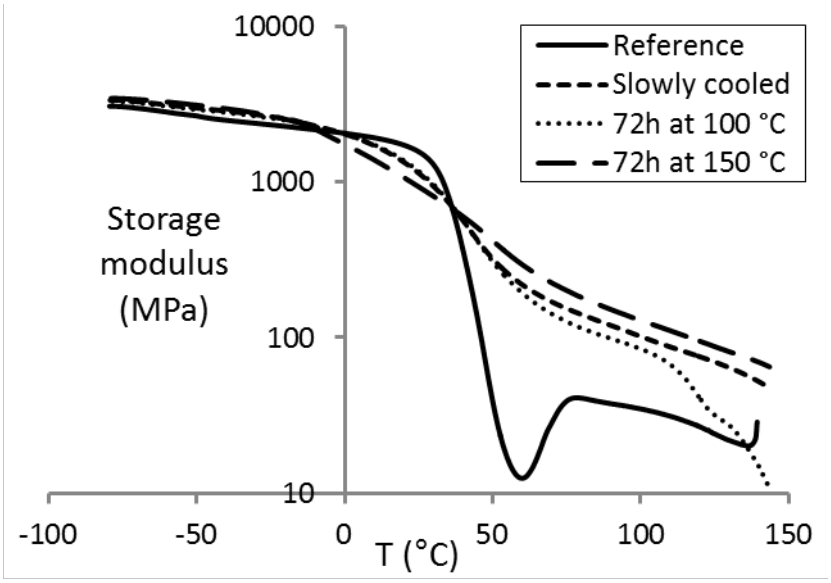

Figure 12: Storage modulus as a function of temperature for the four TPUs with different thermal history.

4 Conclusion

The investigated TPU with a high hard segment content crystallises rather slowly. Crystallinity can be avoided by cooling rapidly down to below the glass transition

Polymer 81 (2015) p. 1-11
DOI: 10.1016/j.polymer.2015.11.007
temperature. However, crystallisation is induced during reheating. This type of crystallisation induces a disordered domain morphology as suggested by modelling of the SAXS patterns. Semicrystalline species at room temperature are obtained by cooling rather slowly or by annealing rapidly cooled materials at a sufficiently high temperature. The level of disorder depends on the thermal history. During slow cooling, a disordered morphology is favoured, while during annealing 12-15% of the material volume adopts a lamellarly ordered morphology. The differences in morphology as a function of thermal history and temperature correlated well with changes in the storage modulus.

Based on SAXS and WAXD measurements, the multiple endotherms in the investigated TPU were attributed to the presence of two polymorphs. The complexity in thermal behaviour is further increased by annealing effects and recrystallisation phenomena. Stiffer TPUs can be obtained by tweaking the morphology towards higher crystallinities and more ordered phase separated morphologies. This can be exploited by applying suitable thermal histories.

5 Acknowledgements

The authors thank the staff of DUBBLE at the ESRF in France for assisting in the SAXS and WAXD measurements. FWO-Vlaanderen is gratefully acknowledged for supporting the ESRF/DUBBLE Big Science project (G.0C12.13). I. Verpoest holds the Toray Chair in Composite Materials at KU Leuven.

6 References

1. Garrett JT, Siedlecki CA, and Runt J. Macromolecules 2001;34(20):7066-7070.
2. Saiani A, Rochas C, Eeckhaut G, Daunch WA, Leenslag JW, and Higgins JS. Macromolecules 2004;37(4):1411-1421.
3. Li C, Liu J, Li J, Shen F, Huang Q, and Xu H. Polymer 2012;53(23):5423-5435.
4. Li C, Han J, Huang Q, Xu H, Tao J, and Li X. Polymer 2012;53(5):1138-1147.
5. Hood MA, Wang B, Sands JM, La Scala JJ, Beyer FL, and Li CY. Polymer 2010;51(10):2191-2198.
6. Qi HJ and Boyce MC. Mechanics of Materials 2005;37(8):817-839.
7. Skarja GA and Woodhouse KA. Journal of Applied Polymer Science 2000;75(12):1522-1534.
8. Aou K, Ge S, Mowery DM, Zeigler RC, and Gamboa RR. Polymer 2015;56(0):37-45.
9. He Y, Xie DL, and Zhang XY. Journal of Materials Science 2014;49(21):7339-7352.
10. He Y, Zhang X, and Runt J. Polymer 2014;55(3):906-913.
11. Saiani A, Daunch WA, Verbeke H, Leenslag JW, and Higgins JS. Macromolecules 2001;34(26):9059-9068.
12. Hu WC and Koberstein JT. Journal of Polymer Science Part B: Polymer Physics 1994;32(3):437-446.
13. Vanbogart JWC, Bluemke DA, and Cooper SL. Polymer 1981;22(10):1428-1438.
14. Blackwell J and Lee CD. Journal of Polymer Science Part B: Polymer Physics 1984;22(4):759-772.
15. Bagdi K, Molnar K, Wacha A, Bota A, and Pukanszky B. Polymer International 2011;60(4):529-536.
16. Martin DJ, Meijs GF, Gunatillake PA, McCarthy SJ, and Renwick GM. Journal of Applied Polymer Science 1997;64(4):803-817.
17. Seymour RW and Cooper SL. Journal of Polymer Science Part C: Polymer Letters 1971;9(9):689-&.

Polymer 81 (2015) p. 1-11
DOI: 10.1016/j.polymer.2015.11.007
18. Clough SB, Schneider NS, and King AO. Journal of Macromolecular Science, Part B: Physics 1968;2(4):641-648.
19. Samuels SL and Wilkes GL. Journal of Polymer Science Part C-Polymer Symposium 1973(43):149-178.
20. Briber RM and Thomas EL. Journal of Macromolecular Science, Part B: Physics 1983;B22(4):509-528.
21. Seymour RW and Cooper SL. Macromolecules 1973;6(1):48-53.
22. Vanbogart JWC, Gibson PE, and Cooper SL. Journal of Polymer Science Part B: Polymer Physics 1983;21(1):65-95.
23. Chen TK, Shieh TS, and Chui JY. Macromolecules 1998;31(4):1312-1320.
24. Gommes CJ and Goderis B. Journal of Applied Crystallography 2010;43:352-355.
25. Chentsai CHY, Thomas EL, Macknight WJ, and Schneider NS. Polymer 1986;27(5):659-666.
26. Gomand SV, Lamberts L, Gommes CJ, Visser RGF, Delcour JA, and Goderis B. Biomacromolecules 2012;13(5):1361-1370.
27. Goderis B, Reynaers H, Koch MHJ, and Mathot VBF. Journal of Polymer Science Part B-Polymer Physics 1999;37(14):1715-1738.
28. Wilhelm C and Gardette JL. Polymer 1998;39(24):5973-5980.
29. D'Hollander S, Gommes CJ, Mens R, Adriaensens P, Goderis B, and Du Prez F. Journal of Materials Chemistry 2010;20(17):3475-3486.